Atomistic theory of electronic and optical properties of InAsP/InP nanowire quantum dots

Cygorek, Moritz; Korkusinski, Marek; Hawrylak, Pawel

Publisher's version / Version de l'éditeur:
https://doi.org/10.1103/PhysRevB.101.075307
Physical Review B, 101, 7, 2020-02-20

Atomistic theory of electronic and optical properties of InAsP/InP nanowire quantum dots

Moritz Cygorek,[1] Marek Korkusinski,[1,2] and Pawel Hawrylak[1]
[1]*Department of Physics, University of Ottawa, Ottawa, Canada K1N 6N5*
[2]*Security and Disruptive Technologies, National Research Council of Canada, Ottawa, Canada K1A OR6*

(Received 21 October 2019; revised manuscript received 31 January 2020; accepted 4 February 2020; published 20 February 2020)

We present here an atomistic theory of the electronic and optical properties of hexagonal InAsP quantum dots in InP nanowires in the wurtzite phase. These self-assembled quantum dots are unique in that their heights, shapes, and diameters are well known. Using a combined valence-force-field, tight-binding, and configuration-interaction approach we perform atomistic calculations of single-particle states and excitonic, biexcitonic, and trion complexes as well as emission spectra as a function of the quantum dot height, diameter, and As versus P concentration. The atomistic tight-binding parameters for InAs and InP in the wurtzite crystal phase were obtained by *ab initio* methods corrected by empirical band gaps. The low energy electron and hole states form electronic shells similar to parabolic or cylindrical quantum confinement, only weakly affected by hexagonal symmetry and As fluctuations. The relative alignment of the emission lines from excitons, trions, and biexcitons agrees with that for InAs/InP dots in the zincblende phase in that biexcitons and positive trions are only weakly bound. The random distribution of As atoms leads to dot-to-dot fluctuations of a few meV for the single-particle states and the spectral lines. Due to the high symmetry of hexagonal InAsP nanowire quantum dots the exciton fine structure splitting is found to be small, of the order a few μeV with significant random fluctuations in accordance with experiments.

DOI: 10.1103/PhysRevB.101.075307

I. INTRODUCTION

Semiconductor quantum dots [1,2] are promising structures for quantum devices for quantum technologies, in particular due to their interaction with light. This includes quantum dot lasers [3], single-photon sources [4–7], emitters of entangled photon pairs [8–14] and highly entangled photon cluster states [15,16], and other quantum information applications [17–19]. One major obstacle for the self-assembled semiconductor quantum-dot-based devices is the variation of size, shape, and position of quantum dots [20,21]. This implies that also their electronic and optical properties vary from dot to dot and the necessary selection of dots with the desired characteristics leads to a very small yield of the overall device fabrication process.

One approach to deterministically build quantum dots with specific geometries is the growth of quantum dots in nanowires, where the shape and diameter of the quantum dot is defined by the shape and diameter of the nanowire, and the height as well as the material composition of the dot can be controlled during the vertical growth of the nanowire. In Ref. [22] a selective-area vapor-liquid-solid (VLS) growth technique was employed to fabricate hexagonal $InAs_xP_{1-x}$ quantum dots in InP nanowires. The growth of nanowires with small diameters has been shown to produce pristine crystals in the wurtzite phase with negligible intermixing of zincblende stacking [23]. The high symmetry of the hexagonal nanowire quantum dots results in a strongly reduced exciton fine structure splitting [10,24–26]. As a consequence a very high degree of entanglement of photon pairs emitted from nanowire quantum dots via the biexciton cascade has been demonstrated [10,11]. Furthermore, it is also possible to deterministically grow multiple dots within the same nanowire [27], which allows studying coherent coupling between dots [28].

Because of the recent progress in the fabrication of and experiments on InAsP nanowire quantum dots (for a review cf. Refs. [7,29]) it is highly desirable to be able to understand and atomistically simulate their electronic and optical properties. This is, however, a challenging task for a number of reasons:

First, a typical InAsP nanowire quantum dot [22] with a diameter of 18 nm and a height of 4 nm contains about 40 000 atoms. Because the wave functions leak into the barrier, where they decay exponentially, a much larger computational box with hundreds of thousands of atoms is needed. For larger dots or structures comprised of more than one dot, millions of atoms have to be included in the simulations. Second, the nanowires and dots typically grow in wurtzite crystal structure, whereas bulk InP and InAs form zincblende lattices, hence information about bulk wurtzite materials is scarce. Third, the As atoms in $InAs_xP_{1-x}$ dots are randomly incorporated, which gives rise to strong local fluctuations of the confining potential. Fourth, the lattice mismatch between InAs and InP is about 3% so that strain in the wurtzite structure has to be taken into account. The random incorporation of As atoms will also lead to strong spatial fluctuations of the strain field. Thus, strain should be accounted for atomistically as well.

Some of these challenges have been addressed for self-assembled InAs/InP quantum dots with zincblende structure, which have been studied experimentally [30,31] and theoretically [25,32–35] by a number of groups, including some

of us. Here, however, we are interested in InAs quantum dots in InP nanowires, where the main challenge remains the wurtzite structure of $InAs_xP_{1-x}$ nanowire quantum dots and the scarcity of empirical data. For example, no empirical band structures are available, which are often the starting point of the theoretical description of nanostructures. Furthermore, wurtzite and zincblende phases give rise to qualitatively different band structures with a relevant crystal field splitting in the wurtzite phase and the difference in band gaps between, e.g., wurtzite and zincblende InP of about 80 meV is large enough to enable the formation of polytypic zincblende-wurtzite quantum dots or wells in pure InP nanowires [36]. It is therefore difficult to infer concrete information on wurtzite structures from data on the zincblende phase. For these reasons one has to resort mostly to *ab initio* methods.

So far, $k \cdot p$ theory parameters for InP and InAs in the wurtzite phase have been obtained from DFT calculations in Ref. [37]. On the other hand, atomistic tight-binding calculations of InAs/InP nanowire quantum dots [38–40] and quantum dot molecules [41] have been performed but using parameters for the zincblende crystal phase [42].

In this paper, we develop a description of $InAs_xP_{1-x}$ nanowire quantum dots in the wurtzite phase based on valence-force-field, tight-binding, and configuration-interaction methods. The procedure of the simulations follows that of the computational toolkit QNANO described in Refs. [32,43]. However, for the purpose of this project we have completely refactored the QNANO toolkit and the core elements have been parallelized to run efficiently on computer clusters with tens of thousands of cores enabling simulations involving millions of atoms.

Central for modeling the nanowire quantum dots are the tight-binding parameters, including strain corrections. For InAs and InP, these parameters have been available only for the zincblende crystal phase [42]. Here, we obtain a set of parameters for the wurtzite phase by fits to DFT band structures corrected to reproduce experimentally known band gaps. Using those parameters, we then present simulations of single-particle states and excitonic complexes for typical hexagonal InAsP nanowire quantum dots and study their dependence on the dot height, diameter, As concentration, and profile as well as the effects of the intrinsic randomness of As alloying in the InP matrix.

We find that the single-particle states, in particular the conduction band states, form shells that can be classified according to their angular momentum, e.g., s-, p-, or d-type states, in analogy to lens shaped cylindrical quantum dots [44]. The high symmetry of the quantum dot is reflected in the high symmetry of the charge densities of the single-particle states. Increasing the quantum dot height or diameter reduces the confinement energy and decreases the single particle gap. An increased As concentration results in deeper confinement potentials, which also decreases the single-particle gap. Furthermore, investigations of the consequences of a delayed incorporation of As atoms, which leads to As concentration gradients along the growth direction, show that the gap increases with increasing delay lengths. Calculations of the lowest-energy exciton, biexciton, and trion states predict a characteristic alignment of spectral lines, where the biexciton emission line is below the exciton emission line, the line originating from negatively charged trion lies energetically below the biexciton line, and the positively charged trion is located close to the bright exciton line. The fine structure splitting of the bright exciton states, which is technologically very important, e.g., for the degree of entanglement of emitted photon pairs in the biexciton cascade, is predicted to be about 7 μeV for $InAs_{0.2}P_{0.8}$ dots with a height of 4 nm and a diameter of 18 nm.

The paper is structured as follows: First, we briefly review the valence-force-field, tight-binding, and configuration-interaction approach used for the simulation of quantum dots and we provide details about their numerical implementation. Then, we describe the band structure calculations using DFT, the correction of the band gaps and additional quantities entering the modeling of strained bulk wurtzite InAs and InP. This is followed by a description of the fitting procedure and the tight-binding parameters for InAs and InP in the wurtzite crystal phase. Finally, we present and summarize the results of the simulations for quantum dots.

II. METHODS

To simulate the electronic and optical properties of quantum nanostructures, we employ a combined valence-force-field, tight-binding, and configuration-interaction approach reviewed in more detail in Refs. [32,43]. Here, we only present a brief overview.

A. Strain relaxation

The starting point for the simulations are the approximate positions and elements of every atom in the semiconductor nanostructure. Because there is a significant lattice mismatch of about 3% between InAs and InP, strain effects are important. Therefore, in a first step, the atomic positions are relaxed by minimizing the total elastic energy according to the valence force field (VFF) method [45]

$$\begin{aligned} U = \frac{1}{2}\sum_{i=1}^{N_{\mathrm{at}}} \Bigg\{ & \sum_{j=1}^{nn(i)} \frac{3\alpha_{ij}}{4\left(d_{ij}^0\right)^2}\left[(\mathbf{R}_j-\mathbf{R}_i)^2-\left(d_{ij}^0\right)^2\right]^2 \\ & + \sum_{j=1}^{nn(i)}\sum_{k<j}^{nn(i)} \frac{3\beta_{ijk}}{4d_{ij}^0 d_{ik}^0}\left[(\mathbf{R}_j-\mathbf{R}_i)\cdot(\mathbf{R}_k-\mathbf{R}_i)\right. \\ & \left. -\cos\theta_{ijk} d_{ij}^0 d_{ik}^0\right]^2 \Bigg\}, \end{aligned} \tag{1}$$

where N_{at} is the number of atoms, $nn(i)$ indicates the nearest neighbors of atom i, $\mathbf{R}_i$ is the position of atom i, d_{ij}^0 is the equilibrium bond length, and θ_{ijk} is the equilibrium bond angle between the bonds ij and jk. Finally, α_{ij} and β_{ijk} are the Keating parameters determining the strengths of the bond stretching and bond bending terms, respectively. The energy minimization is performed numerically using the conjugate-gradient method.

B. Tight-binding calculation

The single-particle states are calculated within a tight-binding approach. Here, we use the spds* model with

$N_{\mathrm{orb}} = 20$ local orbitals per atom and with nearest-neighbor hopping. The corresponding tight-binding Hamiltonian is

$$H_{TB} = \sum_{i=1}^{N_{\mathrm{at}}} \sum_{\alpha=1}^{N_{\mathrm{orb}}} \epsilon_{i,\alpha} c_{i,\alpha}^{\dagger} c_{i,\alpha} + \sum_{i=1}^{N_{\mathrm{at}}} \sum_{\alpha,\beta=1}^{N_{\mathrm{orb}}} \lambda_{i,\alpha,\beta} c_{i,\alpha}^{\dagger} c_{i,\beta} + \sum_{i=1}^{N_{\mathrm{at}}} \sum_{j=1}^{nn(i)} \sum_{\alpha,\beta=1}^{N_{\mathrm{orb}}} t_{i,\alpha,j,\beta} c_{i,\alpha}^{\dagger} c_{j,\beta}, \quad (2)$$

where $\epsilon_{i,\alpha}$ is the onsite energy at orbital α on atom i, $t_{i,\alpha,j,\beta}$ is the hopping matrix element between orbitals α and β on atoms i and j, respectively, and $\lambda_{i,\alpha,\beta}$ describes the spin-orbit interaction [46]. Using the Slater-Koster rules [47], the hopping elements $t_{i,\alpha,j,\beta}$ are calculated from a reduced number of hopping elements, e.g., $V_{sp\sigma}^{ac}$ for the σ bond between the s orbital of an anion and the p orbital of a cation, combined with the cosines of the bond angles. Furthermore, for strained structures, we use a generalized Harrison's law and scale the hopping elements $t_{i,\alpha,j,\beta}$ by a factor $(d_0/d)^{\eta_{\alpha,\beta}}$, where d_0 is the equilibrium bond length, d is the bond length in the strained structure, and $\eta_{\alpha,\beta}$ is the exponent. Similarly, the diagonal energies have to be corrected in the presence of strain, where we use the approach introduced in Ref. [48]

$$\epsilon_{i,\alpha} = \epsilon_{i,\alpha}^{\mathrm{eq}} + \sum_{j=1}^{nn(i)} \sum_{\beta} C_{i\alpha,j\beta} \frac{\left(t_{i\alpha,j\beta}^{\mathrm{eq}}\right)^2 - (t_{i\alpha,j\beta})^2}{(\epsilon_{i\alpha} - \epsilon_{\mathrm{ref}}) + (\epsilon_{j\beta} - \epsilon_{\mathrm{ref}})}, \quad (3)$$

where $\epsilon_{i,\alpha}^{\mathrm{eq}}$ and $t_{i\alpha,j\beta}^{\mathrm{eq}}$ refer to the parameters for an unstrained material, ϵ_{ref} is a reference energy value which we take to be two Rydbergs, $\epsilon_{\mathrm{ref}} = 27$ eV, and $C_{i\alpha,j\beta}$ are the parameters determining the strengths of the diagonal corrections.

In addition to the deformation potential, strain can also generate a piezoelectric field, which has been studied, e.g., for elongated structures such as InAs nanorods in InP nanowires in Refs. [49,50], where fields with a strength of a few mV/nm have been reported. An established method to include the effects of piezoelectricity on the electronic structure in quantum dots [33,51] is to calculate the piezoelectric potential from the induced charge density given by the divergence of the piezoelectric polarization $\rho_p(\mathbf{r}) = -\mathrm{div}\,\mathbf{P}$, where the polarization $P_i = e_{ijk}\epsilon_{jk}$ is obtained from the piezoelectric coefficients e_{ijk} and the strain tensor ϵ_{jk}. In this paper, we are dealing with alloyed structures with about 20% InAs in an InP matrix. In this situation it is common to find single As atoms in a neighborhood composed of InP, so that the local strain field can fluctuate with a magnitude of the full InAs-InP lattice mismatch of ∼3% on the length scale of a single interatomic bond. This poses a challenge for evaluating derivatives as required for the calculation of the divergence of the polarization. On the other hand, due to the small InAs content, the average piezoelectric field is expected to be much smaller than that generated by pure InAs segments. Furthermore, because we mostly focus on the description of quantum dots with small heights, the confinement energy in the growth direction, which is also the main direction of a piezoelectric field [50], strongly suppresses piezoelectrically induced charge separation. Finally, it was shown by Bester *et al.* [52] that for III-V semiconductors nonlinear corrections to the piezoelectric polarization are important and cancel large parts of the linear contributions. For these reasons, we do not consider piezoelectric fields in this paper. Further investigation in this direction may be needed for simulations of quantum nanostructures with significant elongation in the growth direction.

The diagonalization of the tight-binding Hamiltonian yields the single-particle energies as well as the eigenvectors in the form of the coefficients $F(i,k,\alpha)$ of an expansion of the single-electron wave function $\Phi_i(\mathbf{r})$ in terms of the local orbitals

$$\Phi_i(\mathbf{r}) = \sum_{k=1}^{N_{\mathrm{at}}} \sum_{\alpha=1}^{N_{\mathrm{orb}}} F(i,k,\alpha)\phi_{\alpha}(\mathbf{r} - \mathbf{R}_k). \quad (4)$$

Here, $\phi_{\alpha}(\mathbf{r} - \mathbf{R}_k)$ is the local atomistic orbital centered at atom k. When needed, we approximate the radial part of these orbitals by the Slater formula, however its explicit functional form is not essential for the construction of the single-particle Hamiltonian.

C. Many-body calculation

The optical properties of quantum dots are determined by excitons, trions, and other excitonic complexes. To calculate these complexes one has to diagonalize the many-body Hamiltonian

$$H_{\mathrm{MB}} = \sum_i E_i^{(e)} c_i^{\dagger} c_i + \sum_p E_p^{(h)} h_p^{\dagger} h_p + \frac{1}{2} \sum_{ijkl} \langle ij|V_{ee}|kl\rangle c_i^{\dagger} c_j^{\dagger} c_k c_l + \frac{1}{2} \sum_{pqrs} \langle pq|V_{hh}|rs\rangle h_p^{\dagger} h_q^{\dagger} h_r h_s - \sum_{iqrl} \left(\langle iq|V_{eh}^{\mathrm{dir}}|rl\rangle - \langle iq|V_{eh}^{\mathrm{exc}}|lr\rangle\right) c_i^{\dagger} h_q^{\dagger} h_r c_l. \quad (5)$$

Here, $c_i^{\dagger}(c_i)$ and $h_p^{\dagger}(h_p)$ refer to creation (annihilation) operators of electrons and holes, respectively, in the basis of the single-particle eigenstates of the tight-binding Hamiltonian. $E_i^{(e)}$ is the energy of the ith electron state and $E_p^{(h)}$ is the energy of the pth hole state, i.e., the negative of the eigenvalue of the tight-binding Hamiltonian for states below the gap. Furthermore, the many-body Hamiltonian contains the electron-electron (V_{ee}), hole-hole (V_{hh}), and electron-hole direct (V_{eh}^{dir}) and exchange (V_{eh}^{exc}) terms of the Coulomb interaction.

To enable the calculation of Coulomb matrix elements for a system with about one million atoms, some approximations have to be made. In particular, we calculate only two-center terms and treat onsite and long-range terms differently. The onsite Coulomb matrix element between Slater orbitals can be precomputed for each material. For the long-range terms we can replace the position difference $|\mathbf{r}_1 - \mathbf{r}_2|$ of electrons or holes by the difference of the positions of the atoms around which orbitals are centered and apply orthogonality relations to solve the remaining integrals. For example, for the electron-

electron term, we arrive at the onsite (OS) and long-range (LR) contributions

$$\langle ij|V_{ee}^{(\mathrm{OS})}|kl\rangle = \frac{e^2}{4\pi\epsilon_0\epsilon_{\mathrm{OS}}}\sum_{a=1}^{N_{\mathrm{at}}}\sum_{\alpha,\beta,\gamma,\delta=1}^{N_{\mathrm{orb}}} F^*(i,a,\alpha)F^*(j,a,\beta) \times F(k,a,\gamma)F(l,a,\delta) \times\left[\int d^3r_1\int d^3r_2\frac{\phi_\alpha^*(\mathbf{r}_1)\phi_\beta^*(\mathbf{r}_2)\phi_\gamma(\mathbf{r}_2)\phi_\delta(\mathbf{r}_1)}{|\mathbf{r}_1-\mathbf{r}_2|}\right], \quad (6a)$$

$$\langle ij|V_{ee}^{(\mathrm{LR})}|kl\rangle = \frac{e^2}{4\pi\epsilon_0\epsilon_{\mathrm{LR}}}\sum_{a_1=1}^{N_{\mathrm{at}}}\sum_{\substack{a_2=1\\a_2\neq a_1}}^{N_{\mathrm{at}}}\sum_{\alpha,\beta=1}^{N_{\mathrm{orb}}}\frac{1}{|\mathbf{R}_{a_1}-\mathbf{R}_{a_2}|} \times F^*(i,a_1,\alpha)F^*(j,a_2,\beta)F(k,a_2,\beta)F(l,a_1,\alpha). \quad (6b)$$

Here, we assume the long-range terms are screened by the bulk dielectric constant $\epsilon_{\mathrm{LR}}=\epsilon$ while the onsite terms are taken as unscreened $\epsilon_{\mathrm{OS}}=1$.

With the Hamiltonian (5) fully parametrized, we can now compute the ground and excited states of four fundamental excitonic complexes: the neutral exciton X, the positively and negatively charged exciton X^+ and X^-, respectively, and the biexciton XX. In each case we form the many-body basis by generating all possible configurations of the electrons and holes on a chosen set of single-particle states. Specifically, the configurations for X take the form $|ip\rangle = c_i^\dagger h_p^\dagger|0\rangle$, where $|0\rangle$ denotes the vacuum state (an empty quantum dot). For X^+ these configurations have the form $|ipq\rangle = c_i^\dagger h_p^\dagger h_q^\dagger|0\rangle$, while for X^- they are $|ijp\rangle = c_i^\dagger c_j^\dagger h_p^\dagger|0\rangle$. Finally, the biexciton states are built in the basis $|ijpq\rangle = c_i^\dagger c_j^\dagger h_p^\dagger h_q^\dagger|0\rangle$. In all these basis configurations, the indices i, j (p, q) enumerate all available electron (hole) single-particle states obeying Fermionic occupation rules.

For each excitonic complex, diagonalization of the Hamiltonian (5) in the appropriate basis gives us the ground and excited states in the form of linear combinations

$$|X_\alpha\rangle = \sum_{i,p} A_{i,p}^\alpha |ip\rangle \quad (7)$$

for the exciton and analogous forms for the other complexes. Here the index α enumerates the excitonic states and $A_{i,p}^\alpha$ are the expansion coefficients of the eigenvector.

D. Optical spectra

One of the ingredients in the calculation of the emission spectra of the excitonic complexes is the dipole element

$$D_{ip}(\boldsymbol{\epsilon}) = \langle i|\mathbf{r}\cdot\boldsymbol{\epsilon}|p\rangle, \quad (8)$$

where $\mathbf{r}$ is the position operator, while $\boldsymbol{\epsilon}$ denotes the polarization of emitted light. This element is computed with the single-particle states of the form as in Eq. (4), respectively, for the electron (i) and the hole (p). Details of calculation of this element in the tight-binding basis are given in Ref. [43]. Utilizing the elements D_{ip} we now define the interband polarization operator

$$P(\boldsymbol{\epsilon}) = \sum_{ip} D_{ip} c_i h_p \quad (9)$$

which removes one electron-hole pair from the system obeying optical selection rules. This operator is central in computing the emission spectra from the state $|\alpha\rangle$ of one of our four excitonic complexes (with N_e electrons and N_h holes). The final state $|f\rangle$ in such a transition is the correlated ground or excited state of the system with N_e-1 electrons and N_h-1 holes. The emission spectrum $F(E,\boldsymbol{\epsilon})$ as a function of the energy E and light polarization $\boldsymbol{\epsilon}$ is computed using Fermi's golden rule

$$F(E,\boldsymbol{\epsilon}) = F_0\sum_{\alpha,f}|\langle\alpha|P(\boldsymbol{\epsilon})|f\rangle|^2\delta[E-(E_f-E_\alpha)]n_\alpha(1-n_f), \quad (10)$$

where F_0 is a constant depending on the light-matter interaction, E_α and E_f are the energies of the many-body states involved in the transition, and n_α and n_f denote the occupations of the respective states. In what follows we focus on the total (unpolarized) emission calculated as the sum $F(E)=F(E,x)+F(E,y)+F(E,z)$ of all possible polarizations. For simplicity we assume that the final states are unoccupied ($n_f=0$) and that due to thermalization only the i_0 lowest-energetic initial states are occupied ($n_\alpha=1$ for $\alpha\leqslant i_0$ and $n_\alpha=0$ for $\alpha>i_0$). Throughout this paper, we focus on the emission predominantly originating from the lowest s-type states, i.e., $i_0=4$ for excitons, $i_0=1$ for biexcitons, and $i_0=2$ for trions. Note that, because the trions consist of an odd number of fermions, the Kramers theorem applies and also the many-body states of trions come in degenerate pairs. Here, we choose to work with those linear combinations of trion states that minimize (maximize) the spin of the unpaired charge carrier.

E. Numerical implementation

In order to be able to use the computational tools developed here not only for the present study of single quantum dots but more generally quantum dot arrays in nanowires, which eventually requires the calculation of systems with millions of atoms, we have completely refactored the toolkit QNANO [32,33,43,53]. We have parallelized the central parts using MPI so that calculations can be performed on hundreds of cores on high-performance computers. For the diagonalization of matrices such as the tight-binding and the many-body Hamiltonian, we use the highly parallelized Krylov-Schur algorithm implemented in the PETSc [54,55]-based library SLEPc [56].

One of the most time consuming steps in our procedure is the calculation of the Coulomb matrix elements. The onsite terms can be distributed straightforwardly as the contributions from different atoms are independent. The long-range terms can be cast into a form that allows for an efficient calculation in terms of matrix-vector multiplications as layed out in Ref. [53]. Here, we parallelize the procedure by splitting the respective matrix into blocks that are calculated and stored on different nodes.

III. BAND STRUCTURE CALCULATIONS

In order to develop a predictive tool based on the empirical tight-binding method, one would like to obtain the hopping elements, diagonal energies, and strain correction parameters from empirical data. However, in contrast to bulk InAs and InP samples, which grow in the zincblende crystal phase, here, we want to model nanowires in the wurtzite phase, where experimental data, e.g., on the band structure of InAs and InP, is scarce.

Although locally zincblende and wurtzite phases are very similar in that they are tetragonally coordinated with first differences appearing in third-nearest neighbors, significant differences in the band structures are expected: The wurtzite phase shows a crystal field splitting that is absent in zincblende structures and the fundamental energy gap is larger in wurtzite structure by, e.g., 59 meV for InAs [57]. These differences preclude a direct reuse of established tight-binding parameters for zincblende InAs and InP [42].

In order to obtain a set of tight-binding parameters together with the strain correction parameters for wurtzite InAs and InP, we use a fitting procedure to reproduce band structures in bulk systems. The band structures are obtained by *ab initio* methods. We perform DFT calculations using the PBE energy functional in a plane wave basis within the QUANTUM ESPRESSO [58,59] code. In order to capture spin-orbit effects, which are particularly important for modeling the valence bands, we use the full relativistic PAW pseudopotentials with nonlinear core corrections derived by Dal Corso [60]. The band structures are well converged for a $16 \times 16 \times 16$ Monkhorst-Pack k-space grid without offsets and an energy cutoff of 50 Ry. The calculations are performed for several different strained unit cell configurations so that the strain correction parameters can be obtained in a simultaneous fit of multiple band structures. Concretely, we start with ideal wurtzite crystal structures with $c/a = \sqrt{8/3}$ and $u = 3/8$ as reference structures and vary a and c/a independently. Experimental equilibrium lattice constants for zincblende structures, namely $a_0^{zb} = 0.5856$ nm for InP and $a_0^{zb} = 0.6044$ nm for InAs, are taken from Ref. [61]. The equilibrium wurtzite lattice constants that reproduce the same bond lengths as in the zincblende crystals are obtained by $a_0 = a_0^{zb}/\sqrt{2}$.

As DFT calculations underestimate the band gap significantly, we perform a scissors shift of the conduction band states to the empirically known fundamental gaps of $E_g = 1.490$ eV in wurtzite InP [62] and $E_g = 0.477$ eV in wurtzite InAs [57], respectively. For InP, a scissors shift of 0.718 eV is required. For InAs, the gap is so small that the underestimation of the gap in calculations using the PBE functional leads to the prediction of a closed gap. Therefore, we focus the fitting to compressed wurtzite InAs structures with lattice constants close to that of the InP matrix, which is about 3% smaller. Note that the dot region in nanowire quantum dot systems is typically composed of $InAs_xP_{1-x}$ with $x \sim 20\%$. Due to the relatively low As concentration, the As atoms will on average experience an environment with lattice constants closer to that of InP than of InAs. Thus, the compressed InAs lattice is a reasonable starting point for the fitting when the parameters will be used to model nanowire quantum dots.

Furthermore, the zero of energy is ill defined in calculations with periodic boundary conditions containing Coulomb interaction terms proportional to $\frac{1}{r}$. Thus, the band alignments between InAs and InP as well as the alignments for different strain configurations are much more difficult to calculate from first principles. Here, we take the zincblende values of the absolute deformation potentials for the valence band maxima of $a_V^{\mathrm{VBM}} = 1.83$ eV for InP and $a_V^{\mathrm{VBM}} = 1.79$ eV for InAs from Ref. [63] and the natural band offset between InAs and InP at their respective equilibrium lattice constants of $\Delta E_v^{\mathrm{eq}}(\mathrm{InAs}) - \Delta E_v^{\mathrm{eq}}(\mathrm{InP}) = 0.47$ eV from Ref. [64].

Note that there is a significant variation in the literature values of the absolute deformation potentials [65]. Also, DFT calculations reveal that $a_v^{\mathrm{gap}} = dE^{\mathrm{gap}}/d\ln(V)$ deviates visibly from a constant over the range of changes of 3% of the lattice constants. For example, including the scissors shift we obtain the energy gap of wurtzite InAs at 3% compression as $E_g^{-3\%} = 0.960$ eV, while starting from the corrected gap at equilibrium and adding the contribution of the relative deformation potential of the gap $a_v^{\mathrm{CMB}} - a_v^{\mathrm{VMB}}$ from Ref. [63] yields a value of $E_g^{-3\%} = 0.991$ eV. Thus, uncertainty in deformation potentials and band alignments defines the order of magnitude of the error of absolute energies in our strained band structure calculations and can be estimated as ∼30 meV.

IV. PARAMETER FITTING

The fitting of the band structures from the M point to Γ to the A point is performed using a conjugate gradient method with stochastic basin hopping to avoid trapping in shallow local minima. For each material, there are 33 tight-binding parameters for structures in absence of strain and 37 additional strain correction parameters. Due to this large parameter space, many different parametrizations can yield similarly good fits. Also, the target function to be optimized is not unambiguous. For example, the overall widths of the lowest conduction and the highest valence bands span several eV. However, it is highly desirable to model the region around the direct gap close to the Γ point, which determines the low-energy physics as well as the optical properties, with a much better accuracy of a few meV. In order to achieve a good compromise, we first perform an unweighted least-squares fit for the lowest conduction bands and the highest valence bands for 20 evenly spaced points along the M-Γ path and for 10 points along the Γ-A path through the Brillouin zone for a good qualitative overall description of the relevant bands. Then, we successively add increasing weights to achieve a better description at Γ, M, and A as well as at a few discretization points close to Γ in order to reproduce the effective mass. With careful adjustment of the weights the optimization procedure eventually localizes in one minimum, in which we then fine tune the parameters, e.g., by increasing the weights around the Γ point to about 10 000 compared to intermediate points in the Brillouin zone. This makes it possible to gradually bend the bands towards the final result, where we aim at a good compromise between the overall band structure and a resolution at the Γ point with an error of ∼5 meV by shifting regions with larger error to intermediate **k** vectors.

Because there are also local minima in the fitting process that result in unphysical tight-binding parameters, we also fix

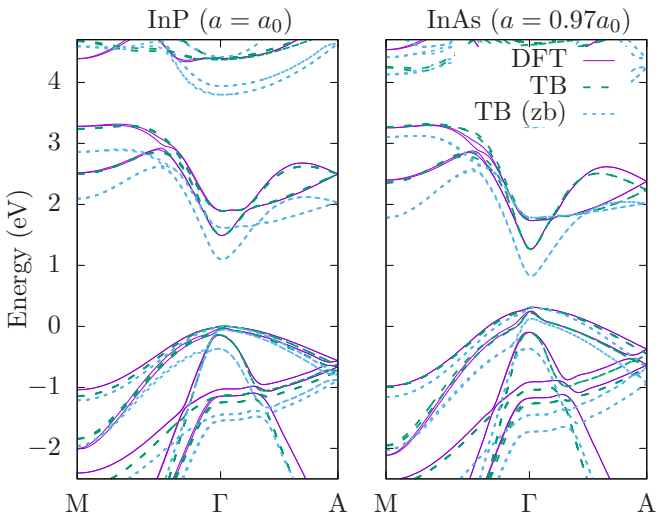

FIG. 1. Band structure of InP (left) in the ideal wurtzite phase at its equilibrium lattice constant $a = a_0$ and of InAs (right) in a hydrostatically compressed ideal wurtzite crystal with lattice constant $a = 0.97a_0$. The DFT calculations have been corrected by scissors shifts. The tight-binding (TB) calculation are obtained from the fitted parameters. For comparison we show tight-binding results [TB (zb)] obtained from the zincblende parameters from Ref. [42], where the energies are shifted so that the valence band maxima coincide with that of the DFT calculations.

the signs of the most important hopping elements, penalize strong deviations of the generalized Harrison's law coefficients $\eta_{i,\alpha}$ from 2, and suppress large values of the diagonal strain corrections. Note also that fitting the band structure through multiple points in k space together with defined symmetries of the local orbitals enables a distinction between terms originating from s, p, or d orbitals. However, the s* orbital, which is designed to model higher lying conduction band states, has the same symmetry as the s orbital, so that s and s* orbitals cannot be distinguished by symmetry in a naive fitting procedure of the band structure. We therefore design the target function to penalize small values of the s* diagonal energy. Finally, to ensure compatibility between the tight-binding parameters for wurtzite InAs and InP, we first obtain the InP parameters and then we use those values as a starting guess for the fit for InAs while reducing the range of the stochastic basin hops to remain in a minimum compatible to the InP parameters.

Figure 1 shows the band structures in the wurtzite phase for InP at its equilibrium lattice constant and InAs with a lattice constant compressed by 3% of its equilibrium value from the M point through Γ to the A point, where scissor shifts have been applied to correct the DFT gap to reproduce the experimental values. The results of the tight-binding calculations for the fitted tight-binding parameters as well as calculations with zincblende InP parameters from Ref. [42] are compared, where in the latter calculation all energies have been shifted so that the valence band maximum coincides with that of the DFT calculations. The fit reproduces the overall DFT band structure well. The calculation using the zincblende parameters on the other hand predicts a smaller band gap and shows qualitative different behavior especially around the valence band maximum due to the lack of a crystal field splitting.

TABLE I. Tight-binding parameters for InP and InAs in the wurtzite phase.

	InP (eV)	InAs (eV)
E_s^a	−3.9798	−5.3673
E_s^c	−1.9268	−0.9905
E_p^a	2.3067	2.3917
E_p^c	6.8862	6.6883
E_{pz}^a	2.3389	2.6082
E_{pz}^c	6.2922	6.0555
E_d^a	13.4134	13.7658
E_d^c	12.2801	12.5896
$E_{s^*}^a$	19.2302	19.5859
$E_{s^*}^c$	19.1728	18.3726
Δ_{so}^a	0.0217	0.1482
Δ_{so}^c	0.1675	0.0645
$V_{ss\sigma}$	−2.6537	−3.5352
$V_{sp\sigma}^{ac}$	3.3428	4.3074
$V_{sp\sigma}^{ca}$	3.3557	3.5224
$V_{pp\sigma}$	3.8437	3.5053
$V_{pp\pi}$	−1.2305	−1.2792
$V_{ss^*\sigma}^{ac}$	−1.3517	−2.5597
$V_{ss^*\sigma}^{ca}$	−3.8673	−5.5423
$V_{s^*s^*\sigma}$	−4.3416	−5.7421
$V_{s^*p\sigma}^{ac}$	2.6263	2.2262
$V_{s^*p\sigma}^{ca}$	3.1080	3.5650
$V_{sd\sigma}^{ac}$	−3.2625	−4.7604
$V_{sd\sigma}^{ca}$	−2.4241	−2.9015
$V_{pd\sigma}^{ac}$	−1.8250	−1.6637
$V_{pd\sigma}^{ca}$	−1.3002	−1.2407
$V_{pd\pi}^{ac}$	1.4239	1.3719
$V_{pd\pi}^{ca}$	1.6504	2.2598
$V_{s^*d\sigma}^{ac}$	−0.7779	−1.2618
$V_{s^*d\sigma}^{ca}$	−0.6759	−1.1917
$V_{dd\sigma}$	−1.8423	−2.3460
$V_{dd\pi}$	3.2696	2.4663
$V_{dd\delta}$	−0.5511	−0.9812

The tight-binding parameters for InP and InAs in the wurtzite phase obtained from our fitting procedure are listed in Table I. The strain parameters, i.e., the Harrison's law exponents η and the diagonal strain corrections C, are shown in Table II. The labels a and c refer to the anion (P/As) and the cation (In), respectively. Except for the spin-orbit splitting parameters Δ_{so}^a and Δ_{so}^c, which are relevant for the p orbitals, the indices refer to the local orbital or the bonds. For example, the onsite energy of the s orbital on an In atom is E_s^c, the Slater-Koster hopping element [47] between between an s orbital on P and a p orbital on an In atom in InP forming a σ bond is denoted by $V_{sp\sigma}^{ac}$. Because of the hermiticity of the

TABLE II. Strain parameters: Harrison's law exponents η and diagonal correction coefficients C.

	InP	InAs
$\eta_{ss\sigma}$	2.5931	1.7590
$\eta^{ac}_{sp\sigma}$	1.6599	2.0673
$\eta^{ca}_{sp\sigma}$	2.0125	2.9042
$\eta_{pp\sigma}$	3.4803	4.4087
$\eta_{pp\pi}$	2.1529	1.7411
$\eta^{ac}_{ss^*\sigma}$	2.3711	2.7047
$\eta^{ca}_{ss^*\sigma}$	1.5276	2.2829
$\eta_{s^*s^*\sigma}$	2.0682	1.8149
$\eta^{ac}_{s^*p\sigma}$	2.4391	1.7442
$\eta^{ca}_{s^*p\sigma}$	2.7750	2.5430
$\eta^{ac}_{sd\sigma}$	2.6314	1.7371
$\eta^{ca}_{sd\sigma}$	2.0122	2.1701
$\eta^{ac}_{pd\sigma}$	1.7862	1.6910
$\eta^{ca}_{pd\sigma}$	1.5977	1.9338
$\eta^{ac}_{pd\pi}$	1.8807	1.7122
$\eta^{ca}_{pd\pi}$	2.2384	2.5487
$\eta^{ac}_{s^*d\sigma}$	1.8903	1.4862
$\eta^{ca}_{s^*d\sigma}$	2.1164	2.0633
$\eta_{dd\sigma}$	2.3844	2.5827
$\eta_{dd\pi}$	2.3570	3.1018
$\eta_{dd\delta}$	2.3391	2.7207
C_{ss}	1.7460	2.8083
C^{ac}_{sp}	3.8895	4.6150
C^{ca}_{sp}	4.3656	4.4938
C_{pp}	0.9416	0.8099
$C^{ac}_{ss^*}$	0.2023	−0.7137
$C^{ca}_{ss^*}$	−0.4574	−0.7256
$C^{ac}_{ps^*}$	−0.4921	0.4052
$C^{ca}_{ps^*}$	0.1400	−0.5372
$C_{s^*s^*}$	−0.4994	−1.3230
C^{ac}_{sd}	0.1546	0.7472
C^{ca}_{sd}	−0.3382	0.6127
C^{ac}_{pd}	−0.5661	−1.2332
C^{ca}_{pd}	−0.0966	0.3289
$C^{ac}_{s^*d}$	−0.4380	−0.9437
$C^{ca}_{s^*d}$	0.6783	0.2654
C_{dd}	−0.8597	−1.5460

tight-binding Hamiltonian, $V^{ac}_{sp\sigma} = V^{ca}_{ps\sigma}$, and $V^{ca}_{ps\sigma}$ is not listed explicitly.

V. RESULTS

Having obtained the tight-binding parameters, we now move on to calculate single-particle states and spectra of typical hexagonal $InAs_xP_{1-x}$ nanowire quantum dots and investigate the influence of random alloying and changes of sizes and As concentrations.

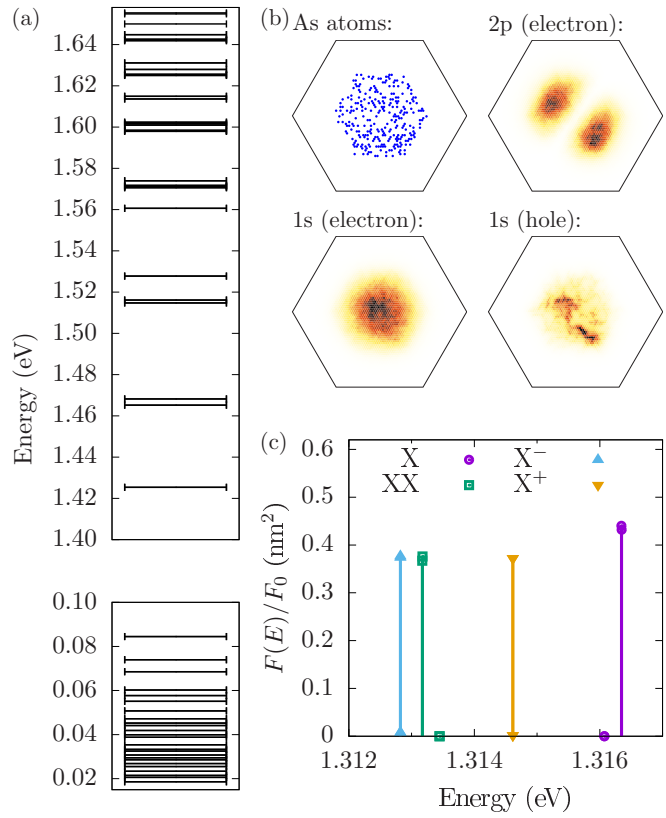

FIG. 2. Single-particle energy eigenstates for a hexagonal $InAs_{0.2}P_{0.8}$ quantum dot with diameter $D \approx 18$ nm and height $d \approx 4$ nm in an InP environment. The energy levels closest to the gap are depicted in (a). (b) shows a horizontal cut though the quantum dot, the distribution of As atoms as well as the densities of single-particle states close to the gap. The spectral lines originating from the lowest-energetic excitons, biexcitons, and trions are depicted in (c).

A. Single-particle states and spectral lines for typical InAsP nanowire quantum dots

A typical hexagonal $InAs_xP_{1-x}$ nanowire quantum dot as grown and described in Ref. [22] has a diameter of $D \approx 18$ nm, a height of $h \approx 4$ nm, and an As concentration of $x = 20\%$. We first present results on one realization of such a dot in Fig. 2. The distribution of As atoms in a horizontal cross section through the computational box is depicted in the top left panel of Fig. 2(b). For all calculations presented here, we use a computational box size containing about 400 000 atoms. For the many-body problem we compute long-range Coulomb matrix elements between 40 electron and hole states and add onsite Coulomb terms between 12 single-particle states per band. Convergence is discussed in detail in Sec. V E.

Figure 2(a) shows the single-particle energy eigenvalues around the gap for this quantum dot, where the energy is defined with respect to the equilibrium bulk wurtzite InP valence band maximum. Note that each line corresponds to two Kramers degenerate pairs due to time-reversal symmetry. A clear shell structure is visible around the gap. In a simplified description assuming a two-dimensional dot with parabolic confinement one expects s-type states followed by two degenerate p-type states. In the atomistic calculations of the

InAsP quantum, we also find two states with similar energies above the lowest conduction band states. To check that not only the energies match the character of s- and p-type states but also the wave functions, we show in Fig. 2(b) the density corresponding to the lowest energetic conduction band state at energy 1.425 eV (1s electron) and the lower of the two states at around 1.465 eV (2p electron). The wave functions in the conduction band are relatively smooth and show clear s- and p-type symmetries, respectively. The density of the second of the pair of p-like states (not shown) is similar to the lower p state but rotated by 90°. Thus, we find that the p-shell states are split in terms of p_x and p_y-like orbitals indicating spatial asymmetry as the cause for the lifting of the degeneracy. This spatial asymmetry is due to the random As distribution in the quantum dot region. It is straightforward to show that a perturbation with hexagonal symmetry to a Hamiltonian with cylindrical symmetry cannot lift the degeneracy of p-type states, because it only couples states that differ by an angular momentum equal to a multiple of three, e.g., f-shell states. The hexagonal confinement potential is therefore ruled out as a cause for the p-shell splitting.

We also depict in Fig. 2(b) the highest valence band state at energy 0.084 eV (1s hole). In contrast to the conduction band states, the valence band states show some granularity. This is due to the fact that the natural band alignment between InP and InAs leads to a shallow confining potential for conduction band electrons whereas the holes experience a deep confining potential, so that the random incorporation of As atoms has a much more drastic impact on the wave functions for holes. Moreover, the effective mass of holes is much larger than that of electrons, which also contributes to the localization of holes.

In Fig. 2(c), the predicted spectral lines originating from the lowest four exciton states (X), the lowest biexciton state (XX) and the lowest two (Kramers degenerate) trion states (negative X^- and positive X^+) are presented, where the height of the lines correspond to the respective optical transition strengths $|\langle\alpha|P(\epsilon)|f\rangle|^2$ in Eq. (10). For this particular quantum dot, the exciton (X) spectra depicted in Fig. 2(c) reveal two dark states, i.e., states with vanishing optical transition strength $|\langle X|P(\epsilon)|0\rangle|^2 \approx 0$, about 0.3 meV below two bright lines. The splitting between the two dark exciton states is about 0.2 μeV while the fine structure splitting (FSS) of the bright excitons is about 3 μeV.

The lines originating from the biexciton (XX) mirror the behavior of the exciton lines. The biexciton binding energy $\Delta E_B = 2E_{\bar{X}} - E_{XX}$ with respect to the average energy $E_{\bar{X}}$ of the two bright exciton states is about $\Delta E_B = 3$ meV. The trion lines are found to the left and to the right of the biexciton line, where the emission energy of the negative trion is lower than that of the positive trion. This can be traced back to the fact that the holes are more strongly confined than electrons and, thus, the Coulomb repulsion between holes is stronger than the repulsion between electrons.

B. Effects of random As incorporation

Due to the random alloying of As within the InP matrix in an $InAs_xP_{1-x}$ nanowire quantum dot the details of the electronic and optical properties fluctuate from one realization of a quantum dot to another. To investigate the effects of randomness we show in Fig. 3 the spectra for excitons, biexcitons, and trions as in Fig. 2(c) for six nominally identical quantum dots with As concentration $x = 20\%$, diameter 18 nm, and height 4 nm that differ only in the locations of the substitutionally incorporated As atoms.

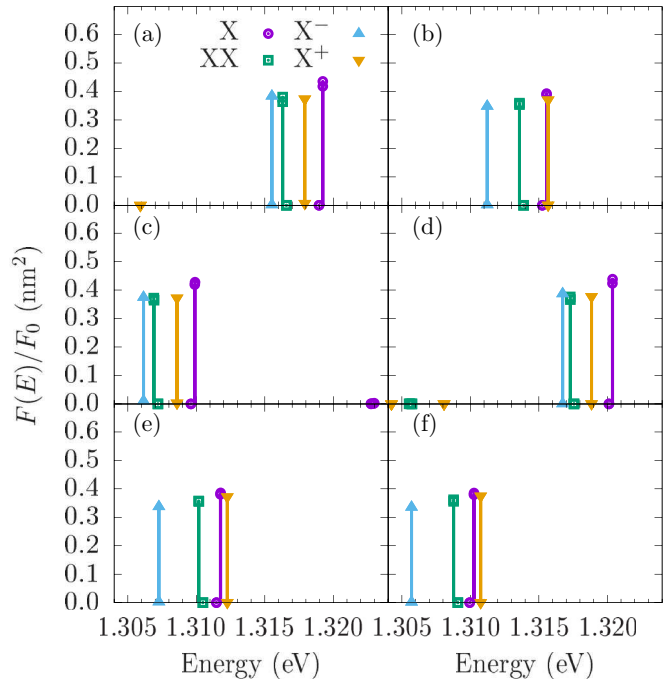

FIG. 3. Spectra of the lowest excitonic complexes for different random realizations of $InAs_{0.2}P_{0.8}$ quantum dots with diameter 18 nm and height 4 nm.

From the calculations we extract an average energy (standard deviation) of the 1s conduction band state of 1.4258 eV (1.8 meV), whereas the highest s-type valence band state is located at 0.0857 eV (2.0 meV). The average splitting (standard deviation) between the lowest s- and p-type conduction band states is 42.2 meV (1.5 meV). The average splitting within the lowest conduction band p-type orbitals is 2.5 meV (1.0 meV), indicating that the splitting in the p shell is dominated by the random As distribution within the quantum dot.

The randomness of alloying affects the many-body states in that the position of the bright exciton line $E(X)$ fluctuates with a standard deviation of 4.1 meV around the mean of 1.3148 eV. The largest contribution to this fluctuation originates from the single-particle states. The exciton binding energy $E_g - E(X)$ and the biexciton binding energy ΔE_B vary with standard deviations of 0.75 meV and 0.72 meV, around the values of 25.3 meV and 2.4 meV, respectively. For the average fine structure splitting of the two lowest bright excitons we find a value of 7.1 μeV with a standard deviation of 4.6 μeV.

For the realizations of quantum dots studied here we always find the biexciton line at lower energies compared with the exciton line and the negative trion line at lower energies compared with the positive trion line. However, whether the positive trion line is found to the left or to the right of the exciton line varies from one random realization to another.

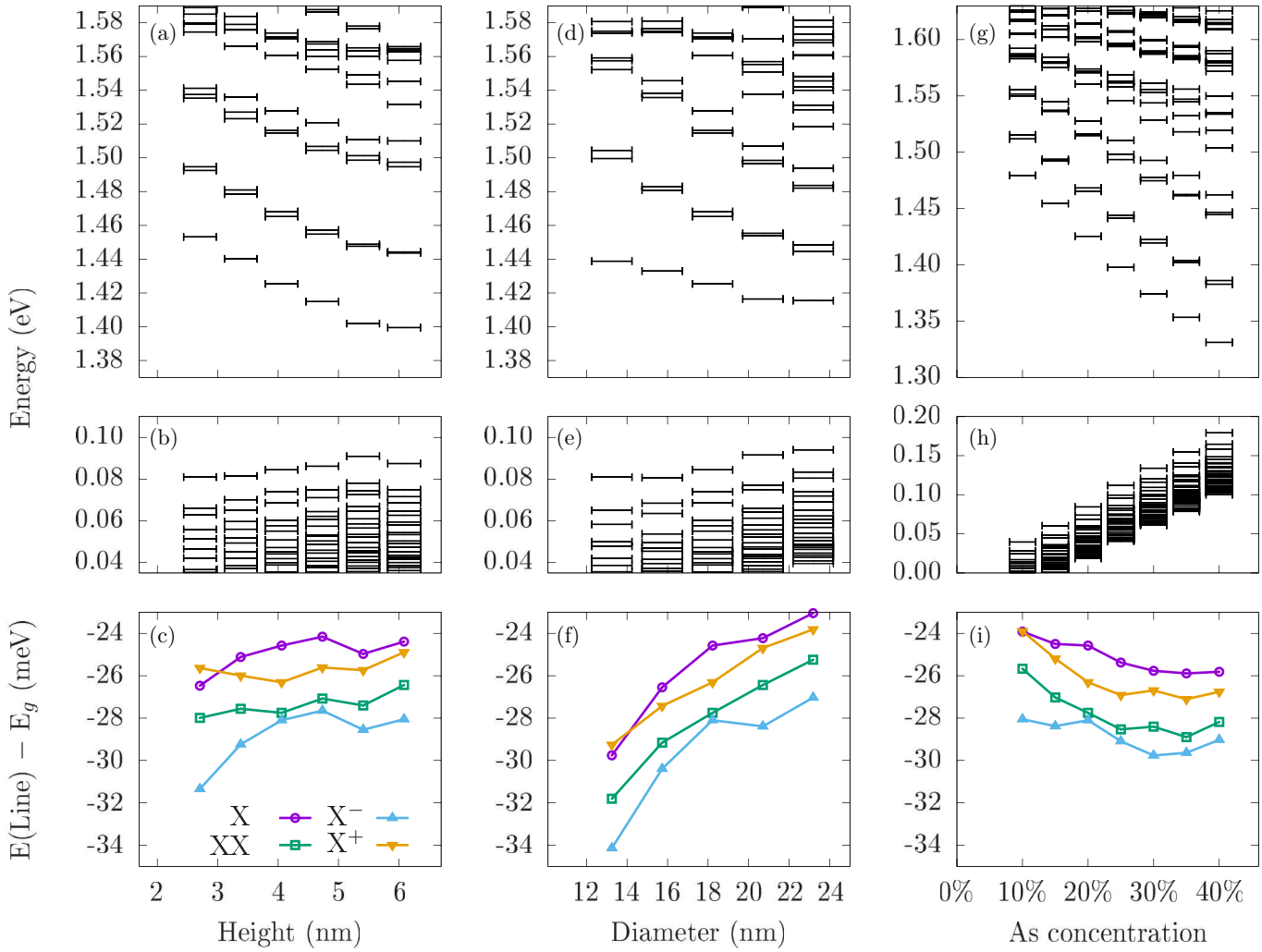

FIG. 4. Dependence of single-particle conduction (first row) and valence band states (second row) on the height (first column), on the diameter (second column) and on the As concentration within the quantum dot (third column). The bottom row shows the positions of the exciton (X), biexciton (XX), and negative (X^-) and positive (X^+) trion lines with respect to the single-particle gap E_g.

It is noteworthy that the relative alignment of the exciton, biexciton, and trion lines qualitatively agrees with tight-binding calculations for cylindrical InAs/InP quantum dots in the zincblende crystal phase [66,67]. Furthermore, empirical pseudopotential calculations comparing lense-shaped zincblende InAs/InP quantum dots with InAs/GaAs quantum dots [35] reveal that embedding InAs dots in a InP matrix leads to more weakly bound biexcitons and positive trions compared with dots in a GaAs environment. This is attributed to the different band alignments between InAs and the respective host material, which leads to more localized hole states in InAs/InP. As a result, the hole-hole Coulomb repulsion is increased, which, for excitonic complexes involving more than one hole, counteracts the binding due to the electron-hole interaction and correlation energy. A clear indication that the same effect is present in InAs/InP dot in the wurtzite phase is the significant splitting between the positive and negative trion lines observed throughout all quantum dots investigated here.

C. Dependence on size and As concentration

Figure 4 summarizes calculations for quantum dots with varying heights, diameters, and As concentrations centered around a prototypical dot of height 4 nm, diameter 18 nm, and As concentration of $x = 20\%$. The single-particle energy levels show typical confinement effects, where the single-particle gap becomes larger for smaller structures, i.e., smaller heights or diameters. The splitting between s- and p-type states remains nearly constant when changing the height of the dot, but it shrinks for increasing diameter, because the s-p-splitting is mainly determined by the lateral confinement. An increased concentration of As atoms leads to effectively deeper confining potentials, reducing the energy of confined particles, which also reduces the effective single-particle gap.

In order to distinguish genuine size-dependent effects of the many-body problem from the confinement effects of the single-particle levels, we plot in the bottom row of Fig. 4 the position of the average bright exciton, biexciton, and trion lines subtracting the respective single-particle gaps E_g.

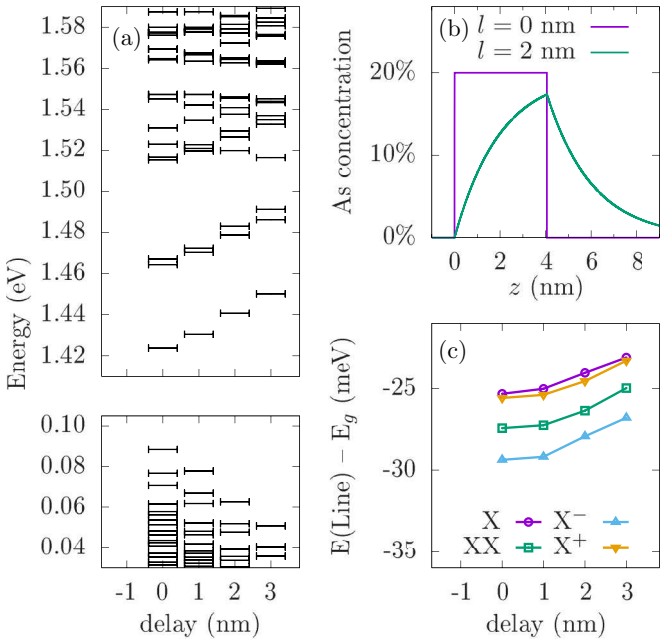

FIG. 5. Delayed incorporation of As atoms (b) and its effect on the single-particle states (a) and spectral lines (c).

The most significant impact of the geometry on the renormalization of the many-body energies due to the Coulomb interaction is found for varying the lateral confinement, where the excitonic complexes tend to be more strongly bound for quantum dots with smaller diameters. This can be explained by the fact that the Coulomb interaction mixes states derived from the s shell with higher lying states. The mixing is strongly influenced by the energetic distance to the remote states. The states that contribute most to the renormalization of s-derived states are the p-type states. Because the splitting between the s and the p shell increases for decreasing diameters, the mixing becomes weaker and the carriers are more strongly forced onto the s shell. This, in turn, increases the Coulomb interaction and leads to stronger renormalizations of the many-body energies. In contrast, the dependence of the many-body energy renormalizations on the quantum dot height or the As concentration is weak. It is noteworthy that within the range of the parameters investigated here, the relative positions of the exciton, biexciton, and trion lines does not depend significantly on the geometry of the quantum dots or the As concentration.

D. Delayed As incorporation

So far, we have discussed hexagonal dots with a uniform As distribution throughout the dot. For such a dot the As concentration is a steplike function of the z coordinate (growth direction) clearly distinguishing the dot region from the surrounding InP environment [cf. concentration for $l = 0$ nm in Fig. 5(b)]. In practice, however, multiple elements in the growth process can act as a buffer. For example, when As is provided to the growth chamber, the chamber itself and the gold droplet used as a growth catalyst still contain excess P atoms. The excess P content can be expected to decay exponentially with some delay length l as P and As atoms are incorporated into the nanostructure. Similarly, after switching off the As supply, the excess As content decays exponentially. The resulting As concentration as a function of the z coordinate is depicted in Fig. 5(b).

The effects of delayed As incorporation in the dot are hard to estimate in advance because the quantum dot region is no longer clearly defined. The volume with nonzero As content increases but the strength of the confining potential decreases. Furthermore, strain effects might obscure the picture. Therefore, numerical studies of the effects of delayed As incorporation are necessary.

Figures 5(a) and 5(c) depict the single-particle states as well as the Coulomb renormalization of the lowest-energetic many-body complexes as a function of the delay length l. It is found that with increasing delay length the lowest conduction band levels shift upward while the highest valence band states shift downwards. This indicates that electrons and holes tend to be more confined to the region with maximal As content in structures with delayed As incorporation compared with the situation in dots with a uniform distribution of the same number of As atoms. The many-body energy renormalization is only marginally affected.

E. Convergence

For the simulation of single-particle states one has to define a computational box with a finite size. For excitonic complexes, the configuration-interaction calculation requires a truncation of the number of single-particle states from which the many-body Hilbert space is constructed. Both convergence parameters, the volume or number of atoms in the computational box and the number of single-particle states entering the many-body calculation, might have an impact on the accuracy of the calculations and limit the size of the systems that can be investigated using our numerical toolkit.

Figure 6(a) shows the energies of the 40 lowest conduction and valence band states as a function of the number of atoms in the computational box up to 1.5 million atoms for the same quantum dot as discussed in Fig. 2. The first computational box with about 40 000 atoms consists of only the quantum dot itself. It can be clearly seen that this computational box is not sufficient for an accurate description, because the wave functions significantly leak outside of the quantum dot region. After a box size with about 400 000 atoms, the lowest few energy levels in the conduction band as well as all considered valence band states remain virtually unchanged. However, new levels appear higher in the conduction band around the first d levels. This is due to the fact that, because of the band alignment between InP and InAs, conduction band electrons experience only a shallow confining potential. The new levels correspond to deconfined states and indicate the onset of a continuum of states in the surrounding InP nanowire. However, this has only a marginal quantitative effect on the positions of the spectral lines of excitonic complexes, which are depicted in Fig. 6(b), because the charge density of the deconfined states outside of the dot are spatially separated from the relevant states within the dot.

The convergence of the configuration-interaction calculation as a function of the number of single-particle states taken into account in the basis of Slater determinants is

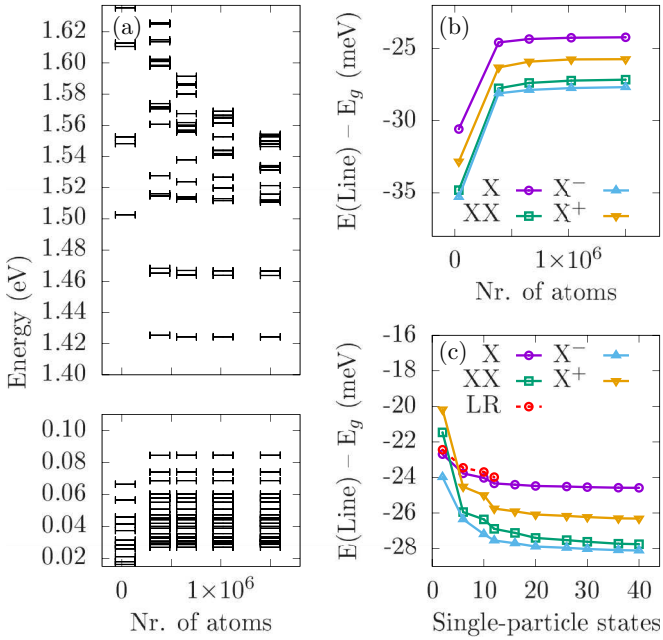

FIG. 6. Conduction and valence band states (a) as well as the lowest-energetic exciton biexciton and trion lines (b) as a function of the number of atoms in the computational box. (c) Evolution of the positions of spectral lines as a function of the number of single-particle states taken into account in the basis for the configuration-interaction calculation.

shown in Fig. 6(c). Note that, because the onsite terms are numerically more demanding, we calculate only Coulomb matrix elements between the 12 single-particle states per band (electrons or holes) for the onsite terms and add them to the long-range Coulomb terms, which we calculate for up to 40 single-particle states per band. For such large structures as the systems under consideration here, the onsite terms have a marginal effect, as can be seen by the positions of the excitons lines denoted as LR and depicted in red in Fig. 6(c), where we only take long-range Coulomb matrix elements into account for the many-body calculation and drop the onsite terms.

The convergence studies suggest that for the discussion of a single InAsP quantum dot a computational box size of about 400 000 atoms is sufficient and convergence of the many-body problem for the lowest-energetic excitonic complexes is reached when 20 single-particle states per band are taken into account.

VI. CONCLUSION

We have presented an atomistic theory of the electronic and optical properties of hexagonal InAsP quantum dots in InP nanowires in the wurtzite phase. We have obtained tight-binding parameters for atomistic simulations of $InAs_xP_{1-x}$ nanowire quantum dots in the wurtzite phase by *ab initio* methods. Using a new, highly parallelized code, we have performed calculations of single-particle states as well as spectra of excitonic complexes for quantum dots with varying sizes and As concentrations as well as different random distributions of As atoms within the dot.

The low energy single-particle states, in particular the conduction band states, form a shell structure and show highly symmetric wave functions that can be classified in terms of s, p, or higher states in close analogy to flat cylindrical quantum dots. While the growth of quantum dots in nanowires allows a fabrication of hexagonal dots with predefined sizes, some residual random fluctuations of the electronic and optical properties, such as the positions of the spectral line in the range of a few meV, are found as a result of the random alloying of As atoms in the InP matrix.

Varying the quantum dot size reproduces characteristic confinement effects, where, e.g., the single-particle gap decreases for larger dots. Similarly, increasing the As/P ratio within the dot leads to deeper confining potentials for electrons and hole and, thus, to a reduced single-particle gap. Furthermore, when the distribution of As atoms along the growth direction is smeared out because of a delayed incorporation of As atoms during the growth process, we find the gap to increase.

The simulation of excitonic complexes such as excitons, biexcitons, and trions consistently predicts spectral lines where the biexciton binding energy is positive and varies with a standard deviation of 0.7 meV about the mean value of 2.4 meV, the negative trion is lower in energy than the biexciton line and positive trion is higher in energy compared to the biexciton, while the positive trion is close to the bright exciton line. Varying the parameters of the quantum dot has only a minor influence on the Coulomb renormalization of the energies of many-body complexes, but affects excitons, biexcitons, and trions in a similar way, so that we cannot identify an unambiguous fingerprint of the geometrical properties on, e.g., the relative positions of the spectral lines originating from different complexes.

For hexagonal or disk-shaped [111] grown nanowire quantum dots, the fine structure splitting between the bright exciton states has been predicted to vanish on grounds of symmetry in Ref. [24]. Our calculations predict an average fine structure splitting of 7.1 μeV with a standard deviation of 4.6 μeV. This is in line with atomistic tight-binding calculations for cylindrical InAsP quantum dots using zincblende parameters [68]. In Ref. [10] the fine structure splitting for a number of nanowire quantum dots has been obtained experimentally yielding a mean of 3.4 μeV with a standard deviation of 3.0 μeV.

An experimental spectra of a wurtzite InAsP nanowire quantum dot is presented in Fig. 1 of Ref. [11]. The exciton line is located at 1.388 eV. The biexciton binding energy is positive and around 2.2 meV. The negative trion line is found to be lower in energy than the biexciton line while the positive trion is slightly above the exciton line. The fine structure splitting for the dot in Ref. [11] is 3.3 μeV. Thus, the relative positions of the spectral lines for this dot agrees well with our predictions.

However, some nanowire quantum dots have also been reported [22] to show negative biexciton binding energies of about −1.5 meV and a number of effects have not yet been accounted for in the modeling. For example, studies of laser-induced atom intermixing [69] highlight the possibility

of diffusion processes and suggests the existence of some defects. Furthermore, as in Stranski-Krastanov-grown quantum dots, there may be a tendency for As atoms to cluster so that the distribution is no longer uniform within one monolayer.

The tight-binding parameters obtained here pave the way for further studies in this direction. Furthermore, our convergence studies have proven the feasibility of simulations with more than one million atoms, which is sufficient to investigate nanowires with two or more quantum dots.

ACKNOWLEDGMENTS

M.C. gratefully acknowledges funding from the Alexander-von-Humboldt foundation through a Feodor-Lynen research fellowship. P.H. and M.C. thank NSERC QC2DM Project and uOttawa Chair in Quantum Theory of Materials, Nanostructures and Devices for support. P.H. and M.C. acknowledge computational resources provided by Compute Canada. Discussions with D. Dalacu, P. Poole, and D. Gershoni are acknowledged.

[1] P. Hawrylak and M. Korkusinski, Electronic and optical properties of self-assembled quantum dots, in *Single Quantum Dots: Fundamentals, Applications, and New Concepts* (Springer-Verlag, Berlin, Heidelberg, 2003), pp. 25–92.
[2] L. Jacak, P. Hawrylak, and A. Wojs, *Quantum Dots* (Springer-Verlag, Berlin, Heidelberg, 1998).
[3] Y. Arakawa and H. Sakaki, Appl. Phys. Lett. **40**, 939 (1982).
[4] P. Michler, A. Kiraz, C. Becher, W. V. Schoenfeld, P. M. Petroff, L. Zhang, E. Hu, and A. Imamoglu, Science **290**, 2282 (2000).
[5] M. Cosacchi, F. Ungar, M. Cygorek, A. Vagov, and V. M. Axt, Phys. Rev. Lett. **123**, 017403 (2019).
[6] C. Santori, M. Pelton, G. Solomon, Y. Dale, and Y. Yamamoto, Phys. Rev. Lett. **86**, 1502 (2001).
[7] H. Mäntynen, N. Anttu, Z. Sun, and H. Lipsanen, Nanophotonics **8**, 747 (2019).
[8] A. Orieux, M. A. M. Versteegh, K. D. Jöns, and S. Ducci, Rep. Prog. Phys. **80**, 076001 (2017).
[9] R. M. Stevenson, R. J. Young, P. Atkinson, K. Cooper, D. A. Ritchie, and A. J. Shields, Nature (London) **439**, 179 (2006).
[10] M. A. M. Versteegh, M. E. Reimer, K. D. Jöns, D. Dalacu, P. J. Poole, A. Gulinatti, A. Giudice, and V. Zwiller, Nat. Commun. **5**, 5298 (2014).
[11] A. Fognini, A. Ahmadi, M. Zeeshan, J. T. Fokkens, S. J. Gibson, N. Sherlekar, S. J. Daley, D. Dalacu, P. J. Poole, K. D. Jöns, V. Zwiller, and M. E. Reimer, ACS Photonics **6**, 1656 (2019).
[12] M. Cygorek, F. Ungar, T. Seidelmann, A. M. Barth, A. Vagov, V. M. Axt, and T. Kuhn, Phys. Rev. B **98**, 045303 (2018).
[13] T. Seidelmann, F. Ungar, M. Cygorek, A. Vagov, A. M. Barth, T. Kuhn, and V. M. Axt, Phys. Rev. B **99**, 245301 (2019).
[14] M. Korkusinski, M. E. Reimer, R. L. Williams, and P. Hawrylak, Phys. Rev. B **79**, 035309 (2009).
[15] N. H. Lindner and T. Rudolph, Phys. Rev. Lett. **103**, 113602 (2009).
[16] I. Schwartz, D. Cogan, E. R. Schmidgall, Y. Don, L. Gantz, O. Kenneth, N. H. Lindner, and D. Gershoni, Science **354**, 434 (2016).
[17] M. E. Reimer, W. R. McKinnon, J. Lapointe, D. Dalacu, P. J. Poole, G. C. Aers, D. Kim, M. Korkusinski, P. Hawrylak, and R. L. Williams, Phys. E (Amsterdam, Neth.) **40**, 1790 (2008).
[18] D. Cogan, O. Kenneth, N. H. Lindner, G. Peniakov, C. Hopfmann, D. Dalacu, P. J. Poole, P. Hawrylak, and D. Gershoni, Phys. Rev. X **8**, 041050 (2018).
[19] B. Jaworowski, N. Rogers, M. Grabowski, and P. Hawrylak, Sci. Rep. **7**, 5529 (2017).
[20] J. Y. Marzin, J. M. Gérard, A. Izraël, D. Barrier, and G. Bastard, Phys. Rev. Lett. **73**, 716 (1994).
[21] L. Wang, V. Křápek, F. Ding, F. Horton, A. Schliwa, D. Bimberg, A. Rastelli, and O. G. Schmidt, Phys. Rev. B **80**, 085309 (2009).
[22] D. Dalacu, K. Mnaymneh, J. Lapointe, X. Wu, P. J. Poole, G. Bulgarini, V. Zwiller, and M. E. Reimer, Nano Lett. **12**, 5919 (2012).
[23] H. Shtrikman, R. Popovitz-Biro, A. Kretinin, L. Houben, M. Heiblum, M. Bukaa, M. Galicka, R. Buczko, and P. Kacman, Nano Lett. **9**, 1506 (2009).
[24] R. Singh and G. Bester, Phys. Rev. Lett. **103**, 063601 (2009).
[25] L. He, M. Gong, C.-F. Li, G.-C. Guo, and A. Zunger, Phys. Rev. Lett. **101**, 157405 (2008).
[26] E. Kadantsev and P. Hawrylak, Phys. Rev. B **81**, 045311 (2010).
[27] C. Carlson, D. Dalacu, C. Gustin, S. Haffouz, X. Wu, J. Lapointe, R. L. Williams, P. J. Poole, and S. Hughes, Phys. Rev. B **99**, 085311 (2019).
[28] M. Bayer, P. Hawrylak, K. Hinzer, S. Fafard, M. Korkusinski, Z. R. Wasilewski, O. Stern, and A. Forchel, Science **291**, 451 (2001).
[29] D. Dalacu, P. J. Poole, and R. L. Williams, Nanotechnology **30**, 232001 (2019).
[30] D. Dalacu, M. Reimer, S. Fréderick, D. Kim, J. Lapointe, P. Poole, G. Aers, R. Williams, W. Ross McKinnon, M. Korkusinski, and P. Hawrylak, Laser Photonics Rev. **4**, 283 (2010).
[31] J. Yuan, H. Wang, R. P. J. van Veldhoven, J. Wang, T. de Vries, B. Smalbrugge, C. Y. Jin, P. Nouwens, E. J. Geluk, A. Y. Silov, and R. Nötzel, Appl. Phys. Lett. **98**, 201904 (2011).
[32] M. Zieliński, M. Korkusiński, and P. Hawrylak, Phys. Rev. B **81**, 085301 (2010).
[33] W. Sheng and P. Hawrylak, Phys. Rev. B **72**, 035326 (2005).
[34] W. Jaskólski, M. Zieliński, G. W. Bryant, and J. Aizpurua, Phys. Rev. B **74**, 195339 (2006).
[35] M. Gong, W. Zhang, G. Can Guo, and L. He, Appl. Phys. Lett. **99**, 231106 (2011).
[36] K. Ikejiri, Y. Kitauchi, K. Tomioka, J. Motohisa, and T. Fukui, Nano Lett. **11**, 4314 (2011).
[37] P. E. Faria Junior, T. Campos, C. M. O. Bastos, M. Gmitra, J. Fabian, and G. M. Sipahi, Phys. Rev. B **93**, 235204 (2016).
[38] Y.-M. Niquet and D. C. Mojica, Phys. Rev. B **77**, 115316 (2008).
[39] M. Zieliński, Phys. Rev. B **88**, 155319 (2013).
[40] M. Zieliński, Phys. Rev. B **88**, 115424 (2013).
[41] M. Świderski and M. Zieliński, Phys. Rev. B **95**, 125407 (2017).
[42] J.-M. Jancu, R. Scholz, F. Beltram, and F. Bassani, Phys. Rev. B **57**, 6493 (1998).

[43] M. Korkusinski, Atomistic simulations of electronic and optical properties of semiconductor nanostructures, in *Nanoscale Materials and Devices for Electronics, Photonics and Solar Energy*, Nanostructure Science and Technology, edited by A. Korkin, S. Goodnick, and R. Nemanich (Springer International Publishing, Cham, 2015), pp. 149–216.
[44] S. Raymond, S. Studenikin, A. Sachrajda, Z. Wasilewski, S. J. Cheng, W. Sheng, P. Hawrylak, A. Babinski, M. Potemski, G. Ortner, and M. Bayer, Phys. Rev. Lett. **92**, 187402 (2004).
[45] P. N. Keating, Phys. Rev. **145**, 637 (1966).
[46] D. J. Chadi, Phys. Rev. B **16**, 790 (1977).
[47] J. C. Slater and G. F. Koster, Phys. Rev. **94**, 1498 (1954).
[48] T. B. Boykin, G. Klimeck, R. C. Bowen, and F. Oyafuso, Phys. Rev. B **66**, 125207 (2002).
[49] R. Anufriev, N. Chauvin, H. Khmissi, K. Naji, G. Patriarche, M. Gendry, and C. Bru-Chevallier, Appl. Phys. Lett. **104**, 183101 (2014).
[50] F. Boxberg, N. Søndergaard, and H. Q. Xu, Adv. Mater. **24**, 4692 (2012).
[51] O. Stier, M. Grundmann, and D. Bimberg, Phys. Rev. B **59**, 5688 (1999).
[52] G. Bester, X. Wu, D. Vanderbilt, and A. Zunger, Phys. Rev. Lett. **96**, 187602 (2006).
[53] W. Sheng, S.-J. Cheng, and P. Hawrylak, Phys. Rev. B **71**, 035316 (2005).
[54] S. Balay, S. Abhyankar, M. F. Adams, J. Brown, P. Brune, K. Buschelman, L. Dalcin, V. Eijkhout, W. D. Gropp, D. Kaushik, M. G. Knepley, D. A. May, L. C. McInnes, R. T. Mills, T. Munson, K. Rupp, P. Sanan, B. F. Smith, S. Zampini, H. Zhang, and H. Zhang, PETSc Users Manual, Tech. Rep. ANL-95/11 - Revision 3.9 (Argonne National Laboratory, 2018).
[55] S. Balay, W. D. Gropp, L. C. McInnes, and B. F. Smith, in *Modern Software Tools in Scientific Computing*, edited by E. Arge, A. M. Bruaset, and H. P. Langtangen (Birkhäuser Press, Basel, 1997), pp. 163–202.
[56] V. Hernandez, J. E. Roman, and V. Vidal, ACM Trans. Math. Software **31**, 351 (2005).
[57] M. B. Rota, A. S. Ameruddin, H. A. Fonseka, Q. Gao, F. Mura, A. Polimeni, A. Miriametro, H. H. Tan, C. Jagadish, and M. Capizzi, Nano Lett. **16**, 5197 (2016).
[58] P. Giannozzi, S. Baroni, N. Bonini, M. Calandra, R. Car, C. Cavazzoni, D. Ceresoli, G. L. Chiarotti, M. Cococcioni, I. Dabo, A. D. Corso, S. de Gironcoli, S. Fabris, G. Fratesi, R. Gebauer, U. Gerstmann, C. Gougoussis, A. Kokalj, M. Lazzeri, L. Martin-Samos, N. Marzari, F. Mauri, R. Mazzarello, S. Paolini, A. Pasquarello, L. Paulatto, C. Sbraccia, S. Scandolo, G. Sclauzero, A. P. Seitsonen, A. Smogunov, P. Umari, and R. M. Wentzcovitch, J. Phys.: Condens. Matter **21**, 395502 (2009).
[59] P. Giannozzi, O. Andreussi, T. Brumme, O. Bunau, M. B. Nardelli, M. Calandra, R. Car, C. Cavazzoni, D. Ceresoli, M. Cococcioni, N. Colonna, I. Carnimeo, A. D. Corso, S. de Gironcoli, P. Delugas, R. A. DiStasio, A. Ferretti, A. Floris, G. Fratesi, G. Fugallo, R. Gebauer, U. Gerstmann, F. Giustino, T. Gorni, J. Jia, M. Kawamura, H.-Y. Ko, A. Kokalj, E. Küçükbenli, M. Lazzeri, M. Marsili, N. Marzari, F. Mauri, N. L. Nguyen, H.-V. Nguyen, A. O. de-la Roza, L. Paulatto, S. Poncé, D. Rocca, R. Sabatini, B. Santra, M. Schlipf, A. P. Seitsonen, A. Smogunov, I. Timrov, T. Thonhauser, P. Umari, N. Vast, X. Wu, and S. Baroni, J. Phys.: Condens. Matter **29**, 465901 (2017).
[60] A. Dal Corso, Phys. Rev. B **86**, 085135 (2012).
[61] P. Haas, F. Tran, and P. Blaha, Phys. Rev. B **79**, 085104 (2009).
[62] G. Bulgarini, D. Dalacu, P. J. Poole, J. Lapointe, M. E. Reimer, and V. Zwiller, Appl. Phys. Lett. **105**, 191113 (2014).
[63] Y.-H. Li, X. G. Gong, and S.-H. Wei, Phys. Rev. B **73**, 245206 (2006).
[64] Y.-H. Li, A. Walsh, S. Chen, W.-J. Yin, J.-H. Yang, J. Li, J. L. F. Da Silva, X. G. Gong, and S.-H. Wei, Appl. Phys. Lett. **94**, 212109 (2009).
[65] E. S. Kadantsev and P. Hawrylak, Appl. Phys. Lett. **98**, 023108 (2011).
[66] M. Zielinski, Nanoscale Res. Lett. **7**, 265 (2012).
[67] M. Zieliński, Phys. Rev. B **99**, 205402 (2019).
[68] M. Zieliński, Phys. Rev. B **100**, 045309 (2019).
[69] A. Fiset-Cyr, D. Dalacu, S. Haffouz, P. J. Poole, J. Lapointe, G. C. Aers, and R. L. Williams, Appl. Phys. Lett. **113**, 053105 (2018).